WILEY-VCH

3D Microstructured Carbon Nanotube Electrodes for Capturing and Recording Electrogenic Cells

Jordi Cools, Davor Copic, Zhenxiang Luo, Geert Callewaert, Dries Braeken*, and Michael De Volder

[*]   Dr. D. Braeken, J. Cools, and Z. Luo

imec, Department of Life Sciences and Imaging, Kapeldreef 75, 3001 Leuven,

Belgium

E-mail: Dries.Braeken@imec.be

Prof. G. Callewaert and J. Cools

KU Leuven, Department of Cellular and Molecular Medicine, 3001 Leuven, Belgium

Dr. M. De Volder and Dr. D. Copic

Institute for Manufacturing, Department of Engineering, University of Cambridge, 17

Charles Babbage Road, Cambridge, CB3 0FS, United Kingdom

ABSTRACT

Electrogenic cells such as cardiomyocytes and neurons rely mainly on electrical signals for intercellular communication. Microelectrode array (MEA) devices have been developed to both record and stimulate electrogenic cell. This technology is fuels new insights in the operation of electrogenic cells and the operation of the brain, and is particularly suitable for long-term recording of cell signals under low cell stress conditions. To date, microelectrode arrays are relying on flat or needle shaped electrode surfaces, mainly due to limitations in the lithographic processes used to fabricate these electrodes. However, cells are intrinsically three-dimensional (3D), and this paper relies on a previously reported elasto-capillary aggregation process, to create 3D carbon nanotube (CNT) MEAs. We found that CNTs aggregated in well-shaped structures of similar size as cardiomyocytes are particularly interesting for MEA applications. This is because (i) CNT microwells of the right diameter preferentially trap individual cardiomyocytes , which facilitates single cell recording without the need for clamping pf cells or deconvolution of signals, and (ii) once the cells are trapped inside of the CNT wells, this 3D CNT structure is used as an electrode surrounding the cell, which increases the cell-electrode contact area and as a result we found that the recorded output voltages increase significantly(up to more than 200%). Further, our fabrication process allows for a large library of 3D geometries in a scalable fashion, which paves the way for future study of complex interactions between electrogenic cells and 3Drecording electrodes.

MAIN

1. Introduction

Real-time recording of electrical signals is critical to understand electrogenic cell behavior and has been of long-standing interest in the field of electrophysiology, neuroscience, drug screening and the development of new active limb prosthetics. While progress has been made in the development and automatization of the patch clamp technology for *in vitro* recordings of excitable cells,[1] microelectrode arrays (MEAs) featuring a large number of stimulation and recording electrodes offer simultaneous and long-term recordings from hundreds of individual cells. Traditional MEAs usually comprise a limited number of electrodes with a large active surface area (diameter between 10 to 100 μm). However, recent advances using small, compact complementary metal-oxide-semiconductor (CMOS) read-out circuitry have significantly improved the readout of MEAs, with highly sophisticated and dense arrays of tens of thousands of subcellular sized electrodes (up to 60,000).[2–5] Nevertheless, these MEA electrodes are still unable to match the signal quality of patch clamp electrodes because of the extracellular nature of the cell-electrode interface. Improving the biocompatibility of the electrode material and maximizing cell-electrode adhesion and electrical coupling have therefore been the subject of much investigation.[6–8] Some interesting strategies for improved intracellular and extracellular recordings include the use of silicon nanowire as field effect transistors (SiNW-FETs) in 2D arrays [9–11] or even as kinked probes that are internalized in the cell.[12] Also electroactive conducting polymers such as polypyrrole (PPy) and poly(3,4-ethylenedioxythiophene) (PEDOT) received increasing attention, leading to significant advances in e.g. flexible organic bioelectronics.[13–16]

Recently, graphene and carbon nanotube (CNT) based electrodes gained considerable interest for neural and cardiac interfacing,[17–21] as well as implant coatings[22,23] and stem cell therapy.[24–26] Their high surface-to-volume ratio and enhanced electron transfer[27] dramatically lower electrode impedance, resulting in improved cell recording and stimulation.[28,29] The

nanoscale roughness of CNT films provides effective anchoring sites for the cell membrane resulting in tight membrane-nanotube interactions and preferential localization of cells on CNTs.[30] Furthermore, increased synaptic activity and excitability was observed in neurons grown on CNT-coated glass substrates[31] and cultured cardiomyocytes displayed higher proliferative capacity and increased electrical activity.[32] Finally, the surface chemistry of CNTs and graphene can easily be modified to control the interfacial interactions between the electrodes and cells, for instance using UV/O$_3$,[21,33] oxygen plasma treatment,[34] or biochemical adhesion factors.[7]

Previous CNT electrode studies have focused on unorganized CNT thin films and vertically aligned CNT (VACNT) 'forests', either as fully covered or micropatterned substrates[30,35,36] and so far, little effort has been made to optimize the 3D recording environment of cells. However, cells and their native environment are intrinsically three-dimensional (3D) and the importance of presenting cells with 3D surroundings is well-recognized for cell scaffolds [**doi:10.1038/nnano.2010.246**], but to date electrodes for MEA applications are limited to flat or needle-shaped structres. In this paper, we describe the fabrication of different 3D CNT microstructures fabricated on top of metal recording electrodes and we both qualitatively and quantitatively characterize the interactions of the electrodes with electrogenic cells. The 3D CNT structuring process builds on a previously reported elasto-capillary aggregation procedure[37] that combines top-down lithographic patterning with bottom-up capillary self-aggregation. Briefly, VACNT forests are grown from lithographically defined catalyst patterns (see **Figure 1a**). The CNT structures are then exposed to an acetone vapor stream, which condenses and evaporates from the surface of the CNTs, pulling them into closer packing by capillary forces. Van der Waals interactions between the densified CNTs then lock this new CNT arrangement in place. This process has three important benefits for this application: First, the initial shape of the VACNT forest is transformed into a more complex 3D shape during the capillary aggregation process, and depending on the initial shape of the forest, we can fabricate

4

CNT microwells and various bending as well as re-entrant structures.[37,38] Second, while as-grown forests are known to have high lateral flexibility, capillary forming transforms the complete forest into a rigid structure with greater mechanical stiffness(Young's Modulus of about 2 GPa).[39] Finally, these complex CNT structures can be grown directly on low impedance, biocompatible molybdenum (Mo) electrical leads and the capillary aggregation reduces the CNT-electrode resistance.[39] This process only requires standard lithography steps and ambient pressure thermal processing and allows fabricating large CNT arrays in batch.[37,38,40,41] This offers a great opportunity to develop new platforms for cell interfacing, taking advantage of the superior electrochemical and electrical properties of CNTs along with a large library of 3D geometries that can be fabricated by capillary aggregation. In this study, we show that well-shaped CNT microstructures are particularly suitable for cell recording as they are able to preferentially trap one single cell, while simultaneously providing a better recording environment because the cells are surrounded electrically conductive CNTs. The latter significantly improves the extracellular sealing resistance and hence the signal-to-noise ratio (SNR) of output signals.

2. Methods

2.1. MEA Fabrication

The MEA fabrication process is depicted in **Figure 1**a. First, a (100) silicon wafer is coated with 500 nm of thermal chemical vapor deposited (TCVD) SiO_2, and next an array of 225 Mo electrodes (35 x 35 μm squares) is fabricated by sputtering and lift-off patterning. About 28% of these electrodes are connected to outside bond pads *via* electrically conductive Mo leads, the other structures are dummies to provide the cells with a homogeneous surface topology. These structures are then passivated with a second TCVD SiO_2 layer (thickness 300 nm) and next this SiO_2 layer is removed above the electrodes and bond pads by a wet buffered HF etch. Finally, the catalyst layer for CNT synthesis (5 nm of Al and 1 nm of Fe) is deposited by e-beam

5

evaporation and patterned by a second lift-off process. The samples are then transferred to an atmospheric CVD tool for CNT growth (400/100/100 sccm He/H_2/C_2H_4 at 775 °C). A multiwalled VACNT forest with a height of approximately 5 μm is obtained after ~30 seconds growth time, which proved to be firmly attached to the substrate (Figure S1, Supporting Information). Figure S2 (Supporting Information) shows the obtained Raman spectrum. Next, the tangled CNT 'crust' layer [42] on the top is removed by a brief O_2 plasma etch. The substrate is then attached to an aluminum mesh and inverted over a beaker containing boiling acetone. When this solvent condenses on the substrate, it is removed from the beaker and the liquid is allowed to evaporate under ambient conditions. During this process, capillary interactions force the CNTs in a closer packing, which transforms the CNTs in their final 3D geometry. Electrodes without CNT microstructures are also fabricated and serve as reference electrodes. as discussed above, this work focusses on well-shaped 3D CNT microstructures . These are fabricated by densifying VACNT microcylinders[43] as illustrated in Figure 1a. We also tested other less successful electrode arrangements including pillars and bending structures reminiscent of 'flowers' (see Figure 1b). These CNT structures as well as regular VACNT forests were benchmarked against the microwell CNT electrodes (see further).

2.2. Biocompatibility of CNT Microstructures

In this paper, we rely on Mo to contact the CNT structures because this material was previously reported to allow for low contact resistance [add reference to supercap paper]. However, the *in vitro* biocompatibility of Mo-containing substrates, and particularly for MEA-based cell recording platforms, has not been investigated in-depth. In this work, we therefore first verified the biocompatibility between cardiomyocytes and CNT-based Mo electrodes. The cell density in these experiments was chosen such that seeded primary cardiomyocytes form a confluent monolayer that exhibits synchronized contraction. If the number of cells is too low, intercellular mechanical coupling would be significantly disrupted and the waves of depolarization (i.e.

action potentials) will not propagate from cell to cell, hampering the recording of cellular field potentials. Conversely, high cell densities cause the cardiomyocytes to form multilayers or cell clumps which is also unfavorable for the purpose of this study, as multiple cell layers prevent clear visualization of the cell-electrode interaction by means of optical and scanning electron microscopy. As shown in Figure S3 (Supporting Information), primary cardiomyocytes cultured on top of flat, laminin-coated Mo substrates remain viable and exhibit spontaneous rhythmic contractions. The same viability is also observed when the Mo electrodes are fully or partially covered with various 3D CNT microstructures.

3. Results and Discussion

3.1. Influence of the electrode geometry on the cell interaction

As illustrated in **Figure 2**, CNT microwell structures show to be particularly advantageous as they provide a large contact area with the cell. Further, α-Actin filament and cell nucleus stainings reveal a change in the cell − electrode interaction with carying well diameter (see Figure 2): For small 2.5 μm diameter wells, the only patches of the cell membranes attach to the wells, For 10 μm wells, the number of cells adhering to the well increases and a significant fraction of wells contain a single nucleus. Further, for the 20 μm microwells (height of 5 to 7 μm) cells deform to nest inside the well and about 75% of the microwell cavities establish membrane contacts. Of the fraction that contained cell nuclei, 67% harbored one cell nucleus and 33% two or more nuclei. There is, however, no one-to-one correspondence between number of nuclei and number of cells, as primary rat cardiomyocytes are known to be multinucleated, *i.e.* the presence of multiple nuclei within a single cell. For rodents, this conversion of cardiomyocytes from a mononucleate to binucleate phenotype happens in the early postnatal period,[44] *i.e.* the time when our cells are extracted. Based on the volume of the 20 μm microwell and the observed distribution of nuclei, we expect to have approximately always one

cell per well, which is particularly interesting for single cell recording applications. Finally, the majority of wells with a diameter of 30 μm or larger contain 4 or more cell nuclei (Figure 2c). Based on the above observations, the optimal microwell size, defined as the cavity diameter that would accommodate a single cardiomyocyte, is about 20 30 μm. We further suggest that cell nestling is likely a combination of cell entrapment during the initial steps of seeding, and crawling of the cell over the sloped CNT walls to enter the well cavity because during the first hours after cell seeding, cells are known to migrate, settle, and attach [add reference]. Finally, the cardiomyocytes form intercellular connections and organize into an electrically active and contracting monolayer. This trapping of cells, does not seem to influence their viability in our experiments.

Confocal imaging of nestled cells further reveal a spiral pattern of α-actin filaments (**Figure 3**a), likely indicating a spiral actin cytoskeleton organization as reported by Tee *et al.*[45] This pattern can also be observed by live-cell imaging using Fluo-4, where regular and spontaneous cytosolic Ca^{2+} transients of cells follow the shape of the well cavity (Figure 3b). Expression of connexin Cx43 − the main cardiac gap junction protein − is well preserved (Figure 3a) and trapped cells are capable to support propagating waves of action potentials within the cellular monolayer (Figure 3c,d). This is important, because it illustrates that despite their physical confinement in the wells, the nested cells maintain their bioelectrical activity (Figure 3e). Moreover, the overall contractile activity and wave propagation of the full cardiac cell monolayer remains unchanged.

3.1. Electrochemical Characterization

In addition to biocompatibility and the ability to preferentially trap single cells, the 3D CNT electrodes offer a lower electrode impedance. This is an important prerequisite for successful recording of cellular electrical activity, as this leads to low Johnson-Nyquist (*i.e.* thermal) noise levels and hence higher signal-to-noise ratios (SNRs). To analyse the electrode impedance,

electrodes with CNT microstructures are electrochemically characterized using electrochemical impedance spectroscopy (EIS) (**Figure 4**a,b). As expected, EIS data indicates that electrode impedance decreases with the CNT electrode area. On average, the impedance at 1 kHz is 155 $\pm$ 26 kΩ for our bare Mo electrodes and decreases to 64 $\pm$ 18 kΩ for electrodes fully covered by a 1-3 μm tall VACNT forest. Statistically equivalent impedance values are obtained for electrodes with 20 μm diameter CNT microwells (75 $\pm$ 26 kΩ), despite the fact that these structures do not completely cover the full Mo surface below. This is due to the fact that the overall electrode area exposed to the liquid is similar. As expected, electrodes with smaller microwells (2.5 μm), pillars or flowers had lower impedance values compared to bare Mo electrodes, but significantly higher than those of larger microwell- or fully VACNT-covered electrodes (Figure S4, Supporting Information).

3.2. Extracellular Recordings

Finally, the CNT-covered electrodes are used for extracellular electrical recording of primary cardiac cells after 3 days *in vitro* (Figure 4c,d). For comparison, the chip also holds flat Mo reference electrodes amongst the electrodes with CNT microstructures and recorded signals are normalized to the signal picked up by these reference Mo electrodes. Spike amplitudes recorded by bare, flat Mo electrodes range from 170 μV_{pp} to 1.5 mV_{pp} and noise levels are 2.5 to 4 μV_{rms}. 20 μm microwell-electrodes yield robust signals with average spike amplitudes as much as twofold larger (~170%) with occasional overshoots up to 425% better than the reference. This large signal amplification compared to the reference Mo electrode is also clearly observed with intracellular measurements after electroporation of the cell membrane using electrical stimulation (Figure S5, Supporting Information).[3] It is interesting to note that although the impedance at 1 kHz of the 20 μm microwell electrodes is not significantly different from the

fully VACNT-covered electrodes, normalized extracellular amplitudes vary considerably. We believe that the latter is due to the microwell electrodes contacting not only the bottom, but also the sides of the cells.

3.3. Simulation Experiments

To validate our measurements, we estimate the theoretically expected potential signal amplification analytically by adapting the area-contact model described by Joye *et al.* (**Figure 5**).[8] We refer to the Supporting Information for an in-depth description of the calculation. Shortly, our output signal calculation is taking into account the spatial distribution of the electrical characteristics of the cell-electrode interface. Using equivalent electric circuits, the model estimates the voltage at the cell-electrode interface of a cell nestled inside a CNT microwell. Compared to flat electrodes, our simulation data predicts a twofold signal amplification, which is in agreement with our measurements. Moreover, our model is consistent with previous simulation data predicting a significant signal amplitude increase when using electrodes with a confined space active area (pits) compared to a flat electrode with the same active surface area.[46] The measured signal amplitude or output voltage V_{out} is mainly determined by the electrical coupling between the cell and the sensing electrode (R_{seal}). Apart from R_{seal}, another important factor for V_{out} is the proximity of extracellular boundaries to the cell such as grooves and cubic pits, as modeled by Lind et al. using finite-element analysis.[46] With membrane potential changes, the voltage on the external surface of the cellular membrane V_{ext} can be described by Equation (1):

$$V_{ext} = i \cdot R_{ecf} \tag{1}$$

with i the ionic current and R_{ecf} the resistance of the extracellular fluid. Hence, V_{ext} can only be increased by raising R_{ecf} and this can be easily accomplished by reducing the volume of the extracellular fluid.[47,48] One prevalent application of this principle is axonal amplification using microchannels.[49–51]

It is also clear that the actual recorded normalized amplitude values for microwell electrodes vary substantially (Figure 4c). We believe this is because the SNR measurements strongly depend on the proportion of the electrode that is actually in contact with the cells. When our data is corrected for wells that are empty, the average amplification increases from 170% to 210% and is very close to the predicted simulation data. Consequently, as no significant differences in electrical impedance were found between electrodes covered by an unpatterned VACNT forest (Figure 4a) and electrodes with a microwell, the observed signal amplification in cell recording (Figure 4c) is solely due to the 3D electrode configuration, which was also confirmed by our simulation.

3.4. Other electrode geometries

Finally, we also recorded potential fom cardiomyocytes with other 3D CNT structures including simple straight pillars as well as bent pillars in a flower arrangement (CNT flowers, see Figure 1b). In contrast to microwells, cells seeded on CNT flowers tended to grow around the CNT 'petals' (Figure S6, Supporting Information). Consequently, the average SNR improvement was only ~50% compared to bare, flat Mo electrodes. Occasionally, a 200% improvement was also observed for pillars and small 2.5 um wells, which we believe occurs when the cells are by chance positioned exactly on top of the electrode. Thus, the large differences in normalized amplitude are due to the specific cell-electrode interface. The key advantage of the 3D wells developed in this work is that the cells are positioning themselves in the 3D wells which subsequently allows to improve the signal by 200% more reproducibly and without the need for manual positioning of the electrodes.

4. Conclusions

This paper shows for the first time that 3D microwell CNT electrodes offer multiple advantages compared to flat or other microstructured CNT electrodes for recording electrogenic cells. First, the conical frustum shape of the well allows to trap cultured cells right on top of the electrode at the bottom of the well. This procedure does not require any manual manipulations like suction nor the use of dielectrophoresis. Second, by choosing an appropriate well diameter the electrode can be shaped for single-cell trapping. Third, wells not only provide a mechanical support for the cell, but also greatly extent the active surface area of the recording electrode. Carbon nanotubes have the advantage of being excellent conductors, chemically stable and they foster good cell adhesion. The latter is important because most of the cell membrane is intimately adhered to the rough nanotube surface, again favoring biopotential recording and stimulation. Further, the design is scalable since large arrays of electrodes can be fabricated in parallel using standard lithographic processes. Finally, the size and slope of the microwells can be adapted, which allows to optimize these structures to trap other cells and to minimize the interstitial space and hence maximize V_{ext} readouts. In addition, as was previously demonstrated, CNT microwells can be infiltrated with polymers and serve as sacrificial scaffolds to shape various materials.[52] This would pave the road for novel 3D microelectrode designs for simultaneous top and bottom cell recording.

Experimental Section

MEA Fabrication Process: The substrate consisted of a (100) silicon wafer with 500 nm of thermal SiO_2 on top. A 70 nm Mo layer was sputtered and patterned by a standard lift-off process using a combination of lift-off resist LOR 1A and positive photoresist IX845. The square electrodes were 35 x 35 µm and the width of the connection lines was 5 µm. Next, a 300 nm CVD SiO_2 layer was deposited to insulate the circuit paths. In a second photoresist step, the electrodes and bond pads were opened again by a wet etch process in buffered HF. A 5 nm Al and 1 nm Fe catalyst layer were then sequentially deposited by e-beam evaporation. The catalyst

layer was patterned using IX845 and ultrasonic agitation in acetone and isopropyl alcohol. After the CNT growth step and capillary forming, the chips were glued to a printed circuit board (PCB) by a non-conductive epoxy, cured at 150 °C for 1 hour and subsequently wire-bonded (Figure S7, Supporting Information). Wires were protected by a layer of biocompatible epoxy (EPO-TEK 353ND-T, Epoxy Technology) and thermally treated at 100 °C for several hours. Prior to electrochemical characterization and cell cultivation experiments, a glass ring lid was glued to the PCB to form the containment volume chamber.

CNT Growth: Carbon nanotube microstructures were grown in a horizontal tube furnace (22 mm inner diameter, 300 mm heated length) at atmospheric pressure with flows of 400/100/100 sccm $He/H_2/C_2H_4$ at 775 °C. A CNT forest with a height of approximately 5 μm was obtained after ~30 seconds of the growth time. The top 'crust' layer was removed by etching in O_2 plasma for 1 min.

Electrochemical Characterization: Samples were electrochemically characterized using an Autolab PGSTAT302N potentiostat/galvanostat instrument from Metrohm, controlled by the NOVA software (version 1.10, Ecochemie, Netherlands). The setup consisted of a three-electrode system placed inside a Faraday cage: the CNT working electrode, a large-area Pt counter electrode coil, and a Ag|AgCl reference electrode. The electrolyte consisted of a phosphate buffered saline (PBS) solution at room temperature. Electrochemical impedance spectroscopy (EIS) was performed with respect to the open-circuit potential (OCP) and a frequency response analysis (FRA) frequency scan was performed between $1-10^4$ Hz with an AC amplitude of 0.01 V(ms). Prior to electrochemical characterization, samples were shortly exposed to 5 min of UV/O_3 (UVO Cleaner 144AX, Jelight Company Inc.) to improve wettability and to improve the cell-electrode interface by providing a better surface for protein coating and cell attachment. Immediately after electrochemical characterization, samples were prepared for cell seeding and sterilized in 70% ethanol for 30 min. A dry sterilization step overnight at 130 °C was used for samples that were not electrochemically characterized.

Cell Culture: Neonatal rat ventricular cardiomyocytes were harvested from two-day-old Wistar rats. The extracted ventricles were washed in Hank's Balanced Salt Solution (HBSS), followed by overnight incubation at 4 °C in 0.05% trypsin. Next, the tissue was dissociated by adding collagenase for 15 min at 37 °C. Cells were separated through trituration and centrifugation and added to primary cardiomyocyte medium, after which they were pre-plated to allow for selective attachment of remaining fibroblasts. After counting and a final centrifugation step, a desired concentration of cardiomyocytes was added to cell culture medium and seeded on the substrate (75,000 cells/cm^2).

Electrophysiological Experiments: Action potentials were recorded using a preamplifier with blanking circuit (MEA1060-Inv-BC, Multi Channel Systems, Reutlingen, Germany) with a gain of 1100 and a sampling rate of 25 kHz and band-pass filter from 1 Hz to 3 kHz. Each recording session lasted for at least 2 min. Positive first biphasic voltage stimuli (±1.5V, pulse width 200 µs) were delivered by an STG2004 stimulator (Multi Channel Systems, Reutlingen, Germany). Raw data were filtered using a second order Butterworth digital filter with a cutoff frequency of 5000 and 10 Hz.

Fluorescent Imaging and Scanning Electron Microscopy: Relative fluorescent changes in the intracellular calcium concentration were visualized using the fluorescent marker Fluo-4 AM (Invitrogen, Belgium), brought in the cells by ester loading 30 min prior to the experiment. Measurements were done using 494 nm excitation and 516 nm emission filters of an upright Examiner microscope (Carl Zeiss, Belgium). For the actin staining, the cardiomyocytes were fixed in prewarmed formaldehyde fixation buffer for 10 min, washed three times with PBS and permeabilized in 0.1% Triton for 5 min. After another PBS wash, an Alexa Fluor 633 Phalloidin solution (Invitrogen, Belgium) was added for 1 h and finally washed one last time in PBS prior to imaging. Living cells, dead cells and cell nuclei were loaded respectively with Calcein-AM, propidium iodide and Hoechst Stain solution 30 min prior to the experiment. Confocal microscopy was performed using a Carl Zeiss LSM 780 confocal laser scanning microscope.

For scanning electron microscopy (SEM) imaging, cells were dehydrated in increasingly concentrated ethanol solutions (10%; 30%; 50%; 70%; 90%; 100%) and subsequently dried in a liquid CO_2 critical point dryer (Automegasamdri-916B, Tousimis). Next, the samples were sputter-coated with 2 nm of Pt to improve conductance and imaged using SEM (Nova NanoSEM 200, FEI).

Statistical Analysis: Statistical analysis was performed using the JMP 10 statistical discovery software (SAS). Any possible outliers were determined using a Grubbs' test (α = 0.01) and excluded from the data. Normality was examined by means of a Shapiro-Wilk test, and multiple groups were compared using a Tukey's honest significant difference (HSD) test. Statistical difference was reached at p-values ≤ 0.05.

Received: ((will be filled in by the editorial staff))

Revised: ((will be filled in by the editorial staff))

Published online: ((will be filled in by the editorial staff))

References

[1]   M. Martina, S. Taverna, *Patch-Clamp Methods and Protocols*; Martina, M.; Taverna, S., Eds.; Springer New York, 2014.

[2]   D. Braeken, R. Huys, J. Loo, C. Bartic, G. Borghs, G. Callewaert, W. Eberle, *Biosens. Bioelectron.* **2010**, *26*, 1474.

[3]   D. Braeken, D. Jans, R. Huys, A. Stassen, N. Collaert, L. Hoffman, W. Eberle, P. Peumans, G. Callewaert, *Lab Chip* **2012**, *12*, 4397.

[4]   M. E. J. Obien, K. Deligkaris, T. Bullmann, D. J. Bakkum, U. Frey, *Front. Neurosci.* **2015**, *9*, 423.

[5]   J. Dragas, V. Viswam, A. Shadmani, C. Yihui, A. Stettler, M. Radivojevic, J. Muller, A. Hierlemann, In *Frontiers in Neuroscience*; 2016.

[6]   S. Khan, G. Newaz, A comprehensive review of surface modification for neural cell adhesion and patterning. *J. Biomed. Mater. Res. - Part A* **2010**, *93*, 1209–1224.

[7]   A. Blau, *Curr. Opin. Colloid Interface Sci.* **2013**, *18*, 481.

[8]   N. Joye, A. Schmid, Y. Leblebici, *Neurocomputing* **2009**, *73*, 250.

[9]   F. Patolsky, B. P. Timko, G. Yu, Y. Fang, A. B. Greytak, G. Zheng, C. M. Lieber, *Science (80-.).* **2006**, *313*, 1100 LP.

[10]   Q. Qing, S. K. Pal, B. Tian, X. Duan, B. P. Timko, T. Cohen-Karni, V. N. Murthy, C. M. Lieber, *Proc. Natl. Acad. Sci.* **2010**, *107*, 1882.

[11]   J. T. Robinson, M. Jorgolli, A. K. Shalek, M.-H. Yoon, R. S. Gertner, H. Park, *Nat. Nanotechnol.* **2012**, *7*, 180.

[12]   B. Tian, T. Cohen-Karni, Q. Qing, X. Duan, P. Xie, C. M. Lieber, *Science (80-.).* **2010**, *329*, 830.

[13]   M. Berggren, A. Richter-Dahlfors, *Adv. Mater.* **2007**, *19*, 3201.

[14]   P. Fattahi, G. Yang, G. Kim, M. R. Abidian, A review of organic and inorganic biomaterials for neural interfaces. *Adv. Mater.* **2014**, *26*, 1846–1885.

[15] C. Liao, M. Zhang, M. Y. Yao, T. Hua, L. Li, F. Yan, Flexible Organic Electronics in Biology: Materials and Devices. *Adv. Mater.* **2015**, *27*, 7493–7527.

[16] M. Ryu, J. H. Yang, Y. Ahn, M. Sim, K. H. Lee, K. Kim, T. Lee, S. J. Yoo, S. Y. Kim, C. Moon, M. Je, J. W. Choi, Y. Lee, J. E. Jang, *ACS Appl. Mater. Interfaces* **2017**, *9*, 10577.

[17] C. M. Voge, J. P. Stegemann, *J. Neural Eng.* **2011**, *8*, 11001.

[18] E. B. Malarkey, V. Parpura, Applications of carbon nanotubes in neurobiology. *Neurodegener. Dis.* **2007**, *4*, 292–299.

[19] A. Fabbro, M. Prato, L. Ballerini, Carbon nanotubes in neuroregeneration and repair. *Adv. Drug Deliv. Rev.* **2013**, *65*, 2034–2044.

[20] V. Martinelli, G. Cellot, M. Toma, C. S. Long, J. H. Caldwell, L. Zentilin, M. Giacca, A. Turco, M. Prato, L. Ballerini, L. Mestroni, **2013**, 5746.

[21] N. Collaert, C. Mora Lopez, D. J. Cott, J. Cools, D. Braeken, M. De Volder, *Carbon N. Y.* **2014**, *67*, 178.

[22] K. Balani, R. Anderson, T. Laha, M. Andara, J. Tercero, E. Crumpler, A. Agarwal, *Biomaterials* **2007**, *28*, 618.

[23] R. L. Spear, R. E. Cameron, Carbon nanotubes for orthopaedic implants. *Int. J. Mater. Form.* **2008**, *1*, 127–133.

[24] T. R. Nayak, L. Jian, L. C. Phua, H. K. Ho, Y. Ren, G. Pastorin, *ACS Nano* **2010**, *4*, 7717.

[25] M. V Pryzhkova, *Stem Cells Transl. Med.* **2013**, *2*, 376.

[26] E. W. Brunner, I. Jurewicz, E. Heister, A. Fahimi, C. Bo, R. P. Sear, P. J. Donovan, A. B. Dalton, *ACS Appl. Mater. Interfaces* **2014**, *6*, 2598.

[27] J. M. Nugent, K. S. V Santhanam, A. Rubio, P. M. Ajayan, *Nano Lett.* **2001**, *1*, 87.

[28] T. Gabay, M. Ben-David, I. Kalifa, R. Sorkin, Z. R. Abrams, E. Ben-Jacob, Y. Hanein, *Nanotechnology* **2007**, *18*, 35201.

[29]   E. W. Keefer, B. R. Botterman, M. I. Romero, A. F. Rossi, G. W. Gross, *Nat. Nanotechnol.* **2008**, *3*, 434.

[30]   X. Zhang, S. Prasad, S. Niyogi, A. Morgan, M. Ozkan, C. S. Ozkan, *Sensors Actuators, B Chem.* **2005**, *106*, 843.

[31]   G. Cellot, F. M. Toma, Z. Kasap Varley, J. Laishram, A. Villari, M. Quintana, S. Cipollone, M. Prato, L. Ballerini, *J. Neurosci.* **2011**, *31*, 12945.

[32]   V. Martinelli, G. Cellot, F. M. Toma, C. S. Long, J. H. Caldwell, L. Zentilin, M. Giacca, A. Turco, M. Prato, L. Ballerini, L. Mestroni, *Nano Lett.* **2012**, *12*, 1831.

[33]   D. O. H. Teare, N. Emmison, R. H. Bradley, *Langmuir* **2000**, *16*, 2818.

[34]   A. D. Hanson, M. E. Wall, B. Pourdeyhimi, E. G. Loboa, *J. Biomater. Sci. Polym. Ed.* **2007**, *18*, 1387.

[35]   M. J. Roberts, M. K. Leach, M. Bedewy, E. R. Meshot, D. Copic, J. M. Corey, a J. Hart, *J. Neural Eng.* **2014**, *11*, 36013.

[36]   A. Béduer, F. Seichepine, E. Flahaut, I. Loubinoux, L. Vaysse, C. Vieu, *Langmuir* **2012**, *28*, 17363.

[37]   M. De Volder, S. H. Tawfick, S. J. Park, D. Copic, Z. Zhao, W. Lu, a J. Hart, *Adv. Mater.* **2010**, *22*, 4384.

[38]   M. F. L. De Volder, S. Tawfick, S. J. Park, a J. Hart, *ACS Nano* **2011**, *5*, 7310.

[39]   M. F. L. De Volder, S. J. Park, S. H. Tawfick, D. O. Vidaud, a J. Hart, *J. Micromechanics Microengineering* **2011**, *21*, 45033.

[40]   D. Copic, S. J. Park, S. Tawfick, M. F. L. De Volder, A. J. Hart, *Lab Chip* **2011**, *11*, 1831.

[41]   M. De Volder, S. Park, S. Tawfick, a J. Hart, *Nat. Commun.* **2014**, *5*, 4512.

[42]   M. F. L. De Volder, D. O. Vidaud, E. R. Meshot, S. Tawfick, a. John Hart, *Microelectron. Eng.* **2010**, *87*, 1233.

[43]   S. Ahmad, D. Copic, C. George, M. De Volder, *Adv. Mater.* **2016**, *28*, 6705.

[44]   F. Li, X. Wang, J. M. Capasso, a M. Gerdes, *J. Mol. Cell. Cardiol.* **1996**, *28*, 1737.

[45]   Y. H. Tee, T. Shemesh, V. Thiagarajan, R. F. Hariadi, K. L. Anderson, C. Page, N. Volkmann, D. Hanein, S. Sivaramakrishnan, M. M. Kozlov, A. D. Bershadsky, *Nat. Cell Biol.* **2015**, *17*, 445.

[46]   R. Lind, P. Connolly, C. D. W. Wilkinson, R. D. Thomson, *Sensors Actuators B. Chem.* **1991**, *3*, 23.

[47]   J. Clark, R. Plonsey, *Biophys. J.* **1968**, *8*, 842.

[48]   G. E. Loeb, W. B. Marks, P. G. Beatty, *Med. Biol. Eng. Comput.* **1977**, *15*, 195.

[49]   J. J. FitzGerald, S. P. Lacour, S. B. McMahon, J. W. Fawcett, *IEEE Trans. Biomed. Eng.* **2008**, *55*, 1136.

[50]   L. Pan, S. Alagapan, E. Franca, T. Demarse, G. J. Brewer, B. C. Wheeler, *IEEE Trans. Neural Syst. Rehabil. Eng.* **2014**, *22*, 453.

[51]   M. K. Lewandowska, D. J. Bakkum, S. B. Rompani, A. Hierlemann, *PLoS One* **2015**, *10*, 1.

[52]   M. De Volder, S. H. Tawfick, D. Copic, A. J. Hart, *Soft Matter* **2011**, *7*, 9844.
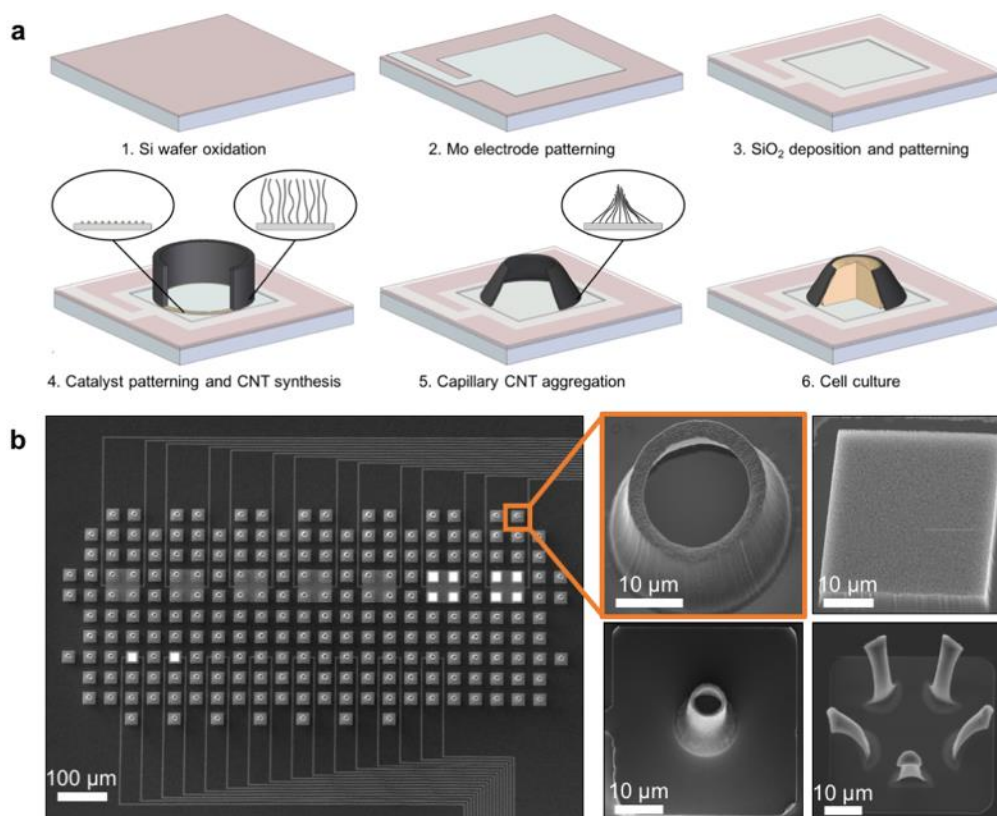
Figure 1. Microelectrode array with microstructured CNT electrodes. a) Schematic representation of the fabrication process. After lithographic patterning of the Mo electrical leads and SiO$_2$ passivation a wet oxide etch is applied to selectively remove the oxide from the electrodes and bond pads. Next, CNTs are grown out of a patterned catalyst layer and transformed into their final 3D geometry using a capillary aggregation process. b) SEM images of the actual MEA layout and some examples of fabricated CNT microstructures including a large and small microwell, a fully CNT covered electrode and a radially-oriented bending structure. Empty Mo squares in between the CNT covered electrodes serve as reference (colored in white).
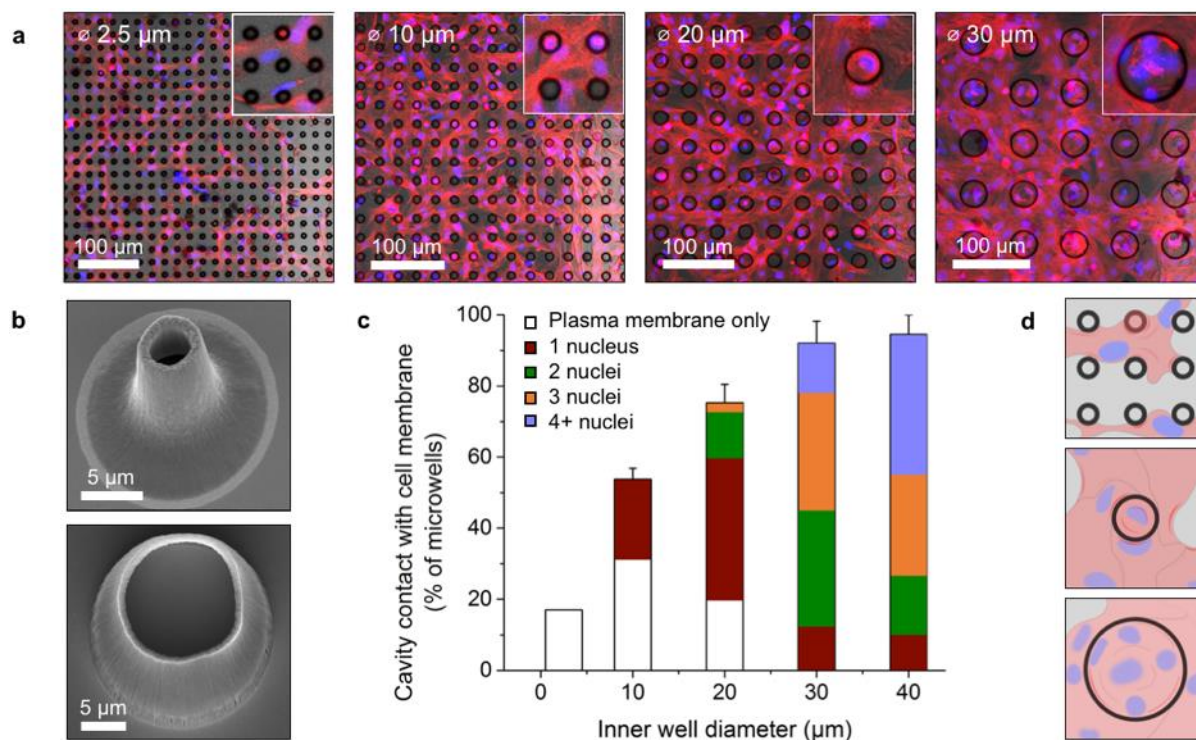
Figure 2. Cardiomyocytes interfacing with CNT microwells. a) Confocal images showing α-actin filaments (red) and cell nuclei (blue) of cardiomyocytes cultured on top of various-sized microwells. b) SEM images of a small 2.5 µm (upper) and medium 20 µm (lower) sized microwell. c) With increasing well diameter the percentage of cells establishing membrane-well contact zones and the number of trapped cell nuclei progressively increases. $n_{2.5} = 441$ [1], $n_{10} = 995$ [6], $n_{20} = 376$ [7], $n_{30} = 50$ [2], $n_{40} = 18$ [2] with n = total number of wells and analyzed number of pictures between brackets. Error bars are SD. d) Model depicting positions of cells growing on small, medium and large microwells.
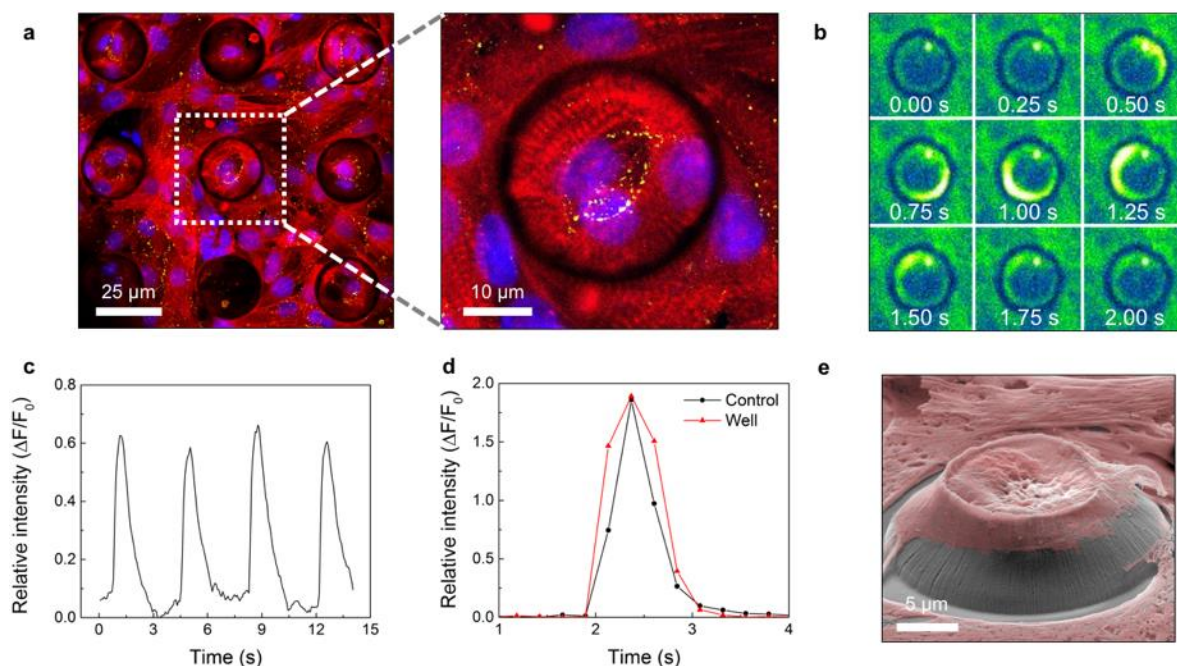
Figure 3. Cardiomyocytes nestled within CNT microwell cavities. a) Confocal image showing α-actin (red), connexin-43 (yellow) and cell nuclei (blue) staining in cardiomyocytes around and within CNT microwells. Enlarged image on the right shows circular patterns of striations − corresponding to sarcomeres − in nestled cells compared to a longitudinal pattern in cells outside of the microwell. b) Time-lapse montage of a cytosolic Ca^{2+} transient of a single cardiomyocyte using the Fluo-4 calcium indicator. c) Quantifying this increase of relative fluorescence intensity over a broader period of time reveals a regular beating pattern in entrapped cells. d) Relative fluorescent intensity over time of two regions of interest (ROIs), i.e. one inside the microwell and another outside and in the vicinity of the well (control), showing that the beating pattern of cells inside a microwell is synchronized to the beating pattern across the whole cellular monolayer. e) Colored SEM image of a primary cardiomyocyte within the cavity of a CNT well.
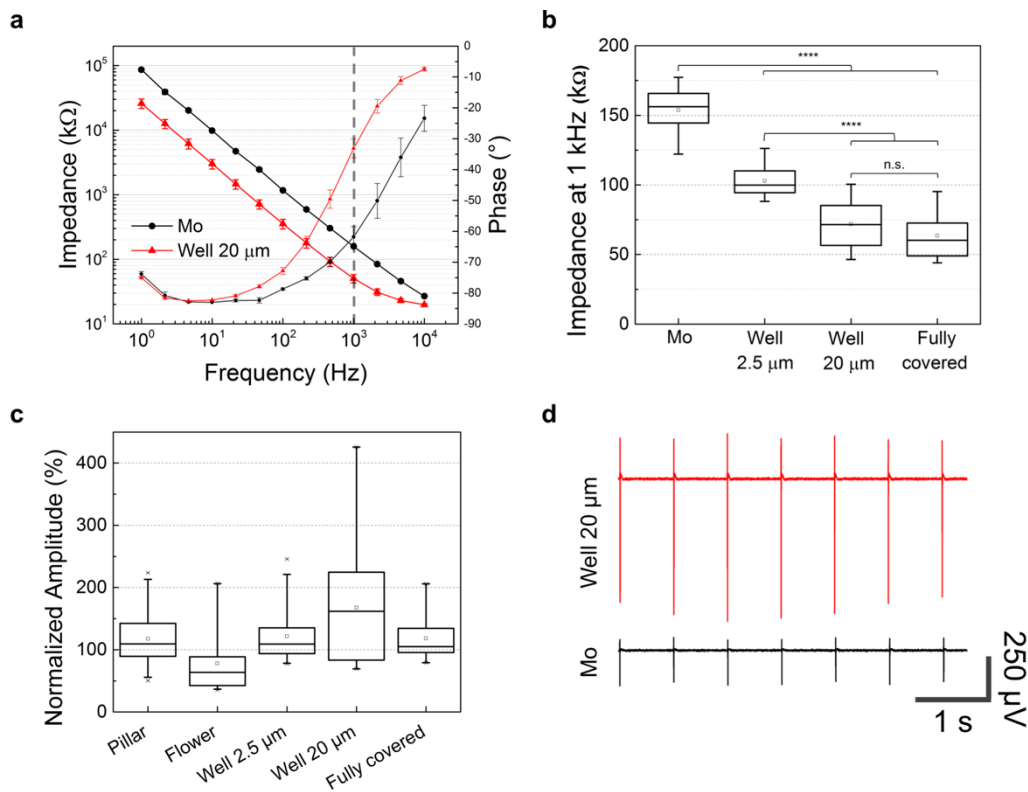
Figure 4. Electrochemical characterization and recording capabilities of CNT-based Mo electrodes. a) Impedance (bold) and phase (thin) plotted as a function of frequency for a bare Mo electrode and with a 20 μm well on top. Dashed line corresponds to 1 kHz. Error bars are SD. b) Impedance data at 1 kHz for bare Mo electrodes ($n = 61$), fully CNT covered electrodes ($n = 28$) and with 2.5 μm ($n = 15$) and 20 μm ($n = 27$) wells on top. Box plots with median, 25th and 75th percentiles; whiskers indicate 10th and 90th percentile and asterisks indicate significant difference with P<0.0001. Impedance of 20 μm wells and fully covered electrodes is not significantly different. c) Normalized amplitudes of cardiac action potentials recorded by various CNT microstructures ($n_{pillar} = 37$, $n_{flower} = 24$, $n_{well2.5} = 20$, $n_{well20} = 18$, $n_{full} = 7$). Box plots with median, 25th and 75th percentiles; whiskers indicate 5th and 95th percentile. d) Typical extracellular signals recorded with a bare Mo electrode (black trace) and 20 μm well electrode (red trace) as a function of time.
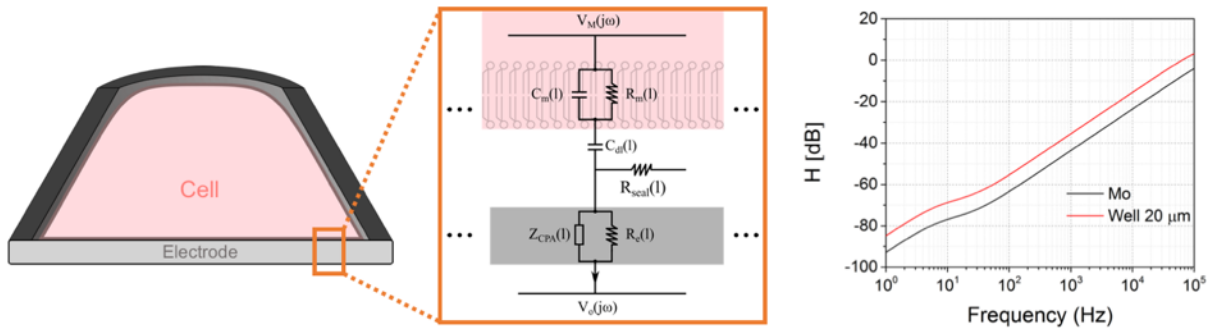
Figure 5. Modeling of the cell-microwell interface. Cross-sectional cartoon of a cell nestled within a microwell (left) and the area-contact model of the cell membrane together with the electrode (middle). $V_M(j\omega)$ is the intracellular potential and $V_o(j\omega)$ the output potential of the electrode. C_m and R_m are the membrane capacitance and resistance, respectively. C_{dl} is the double-layer capacitance, R_{seal} the sealing resistance, Z_{CPA} the constant phase angle element and R_e the electrode resistance. All elements are in function of a distance l from the center of the cell. The simulation result on the right shows the amplitude of the transfer function $H(j\omega)$ in function of the frequency. $H(j\omega)=V_S(j\omega)/V_M(j\omega)$.

Table of Contents Entry

3D carbon nanotube structures are grown on top of microelectrodes and interfaced with primary heart cells. The focus lies on sloped microwells of which the diameter is optimized to allow single cell nestling. Based on microscopy data and cell recordings, these structures seem to hold multiple advantages compared to more traditional electrodes.

Jordi Cools, Davor Copic, Zhenxiang Luo, Geert Callewaert, Dries Braeken, and Michael De Volder*

3D Microstructured Carbon Nanotube Electrodes for Capturing and Recording Electrogenic Cells
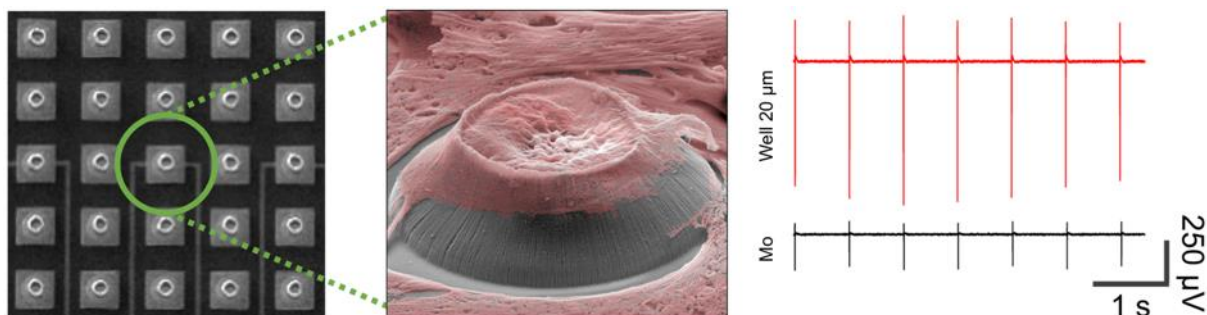
Supporting Information

3D Microstructured Carbon Nanotube Electrodes for Capturing and Recording Electrogenic Cells

Jordi Cools, Davor Copic, Zhenxiang Luo, Geert Callewaert, Dries Braeken*, and Michael De Volder

[*]   Dr. D. Braeken, J. Cools, and Z. Luo
       imec, Department of Life Sciences and Imaging, Kapeldreef 75, 3001 Leuven,
       Belgium
       E-mail: Dries.Braeken@imec.be

       Prof. G. Callewaert and J. Cools
       KU Leuven, Department of Cellular and Molecular Medicine, 3001 Leuven, Belgium

       Dr. M. De Volder and Dr. D. Copic
       Institute for Manufacturing, Department of Engineering, University of Cambridge, 17
       Charles Babbage Road, Cambridge, CB3 0FS, United Kingdom

1. Modeling of the cell-microwell interface

The calculation of the output signal is carried out using the area-contact model which takes into account the spatial distribution of the electrical characteristics of the cell-electrode interface.[1,2]

PART 1 aims at estimating the voltage $V_I(l, j\omega)$ at the cell-electrode interface without considering the electrode, where l is the length of the trajectory between the center of the electrode and an arbitrary position on the cell membrane. A schematic depiction of a cell nestled inside a CNT microwell is show in **Figure S8** and the equivalent electric circuit is shown in **Figure S9**. The corresponding parameters are as follows:

- Area of the infinitesimal membrane segment:

$$\delta A_{ce} = 2\pi R(l)\delta l \tag{1}$$

where $R(l)$ is the distance of an arbitrary point on the cell membrane to the axis of the well structure.

- Cell membrane resistance:

$$r_m(l) = \frac{1}{g_{mem}\delta A_{ce}} \tag{2}$$

- Cell membrane capacitance:

$$c_m(l) = c_{mem}\delta A_{ce} \tag{3}$$

- Cell membrane-electrolyte capacitance:

$$c_{dl}(l) = c_{hd}\delta A_{ce} \tag{4}$$

- Seal resistance:

$$r_{seal}(l) = \frac{\rho}{d}\frac{\delta l}{2\pi R(l)} \tag{5}$$

where ρ is the resistivity of the electrolyte and d is the distance between the cell membrane and the electrode.

According to the equivalent electric circuit, in the Laplace domain V_I satisfies the following equation:

$$\frac{V_I(l,s)-V_I(l-\delta l,s)}{r_{seal}(l-\delta l)} + \frac{V_M(s)-V_I(l,s)}{z_m(l)} = \frac{V_I(l+\delta l,s)-V_I(l,s)}{r_{seal}(l)} \tag{6}$$

With (S1) and:

$$\delta V_I(l,s) = V_I(l,s) - V_I(l-\delta l,s) = V_I(l+\delta l,s) - V_I(l,s) \tag{7}$$

(S6) can be rewritten as:

$$\frac{2\pi d[R(l)-R(l-\delta l)]}{\rho}\frac{\delta V_I(l,s)}{\delta l} = \frac{V_M(s)-V_I(l,s)}{z_m(l)} \tag{8}$$

Finally, with $\delta l \to 0$, we have:

$$\frac{\partial V_I(l,s)}{\partial l} + 2aR(l)V_I(l,s) = 2aR(l)V_M(s) \tag{9}$$

where:

$$a = \frac{s\rho c_{hd}(g_{mem}+sc_{mem})\delta l}{2d[g_{mem}+s(c_{mem}+c_{hd})]\delta R(l)} \tag{10}$$

The cell membrane geometry can be divided into two regions:

Region 1: $L_B < l \le L_T$ where L_B is the radius of the bottom of the cell and L_T is defined as sum of L_B and the side length of the cell L_S

$$L_B = R_w - \frac{d}{\sin\theta} \tag{11}$$

$$L_T = L_B + \frac{h}{\sin\theta} \tag{12}$$

Within region 1:

$$R_1(l) = L_B - (l - L_B)\cos\theta$$

$$\delta R_1(l) = R_1(l) - R_1(l - \delta l) = -\delta l \cos\theta$$

Region 2: $0 < l \leq L_B$

Within region 2:

$$R_2(l) = l \tag{13}$$

$$\delta R_2(l) = R_2(l) - R_2(l - \delta l) = \delta l \tag{14}$$

We solve Equation 9 separately in these two regions and assume that at $l = L_T$ the voltage at the cell-electrode interface $V_I = 0$ and $\lim\limits_{l \to L_B^+} V_I(l, s) = \lim\limits_{l \to L_B^-} V_I(l, s)$

For region 1 ($L_B \leq l \leq L_T$):

$$V_I(l, s) = A_1(s)e^{B_1 l^2 + C_1 l} + V_M(s) \tag{15}$$

where:

$$B_1 = a_1 \cos \theta \tag{16}$$

$$C_1 = -2a_1 L_B(1 + \cos \theta) \tag{17}$$

$$A_1(s) = -\frac{V_M(s)}{e^{B_1 L_T^2 + C_1 L_T}} \tag{18}$$

For region 2 ($0 \leq l \leq L_B$):

$$V_I(l, s) = A_2(s)e^{B_2 l^2 + C_2 l} + V_M(s) \tag{19}$$

where:

$$B_2 = -a_2 \tag{20}$$

$$C_2 = 0 \tag{21}$$

$$A_2(s) = -\frac{A_1(s)e^{B_1 L_B^2 + C_1 L_B}}{e^{B_2 L_B^2 + C_2 L_B}} \tag{22}$$

PART 2: In the second part of the calculation, the electrode is taken into account in the model. The equivalent electric circuit for the electrode is shown in **Figure S10** and the corresponding parameters are as follow:

$$r_e(l) = \frac{r_{ct}}{\delta A_{el}} \tag{23}$$

$$z_{CPA}(l) = \frac{1}{(j\omega c_d)^n} \tag{24}$$

$$c_d(l) = c_{dl}\delta A_{el} \tag{25}$$

$$V_s(s) = Z_{load} \int_0^{R_{el}} \frac{V_I(l,s) - V_s(s)}{z_{el}(l,s)} \tag{26}$$

In our case $R_{el} = L_B$

Replacing $V_I(l, s)$ with Equation 19 and combining Equation 20, 21 and 22, Equation 26 can be rewritten as:

$$V_s(s) = \frac{\pi(1 + r_{ct}(sc_{dl})^n)}{sC_{load}r_{ct} + R_{el}^2\pi(1 + r_{ct}(sc_{dl})^n)} \left[V_M(s)L_B^2 + \frac{A_2}{B_2}(e^{B_2L_B^2} - 1)\right] \tag{27}$$

Parameters:

Electrical parameters:[3–8]

$$\rho = 100 \ \Omega\text{cm}$$

$$c_{hd} = 0.049 \ \text{pF} \ \mu\text{m}^{-2}$$

$$g_{mem} = 0.5 \ \text{S} \ \text{m}^{-2}$$

$$c_{mem} = 20 \ \text{fF} \ \text{um}^{-2}$$

$$r_{ct} = 30 \ \Omega \ \text{m}^{-2} \ (\text{For TiN electrode})$$

$$c_{dl} = 432 \ \mu\text{F} \ \text{cm}^{-2}$$

$$C_{load} = 10 \ \text{pF}$$

Geometrical parameters:

Gap between the cell membrane and the well structure: $d = 70$ nm

Height of the well: $h = 5$ μm

Angle between the well structure and the electrode: $\theta = 60°$

Inner radius of the well structure: $R_w = 11.5 \ \mu m$
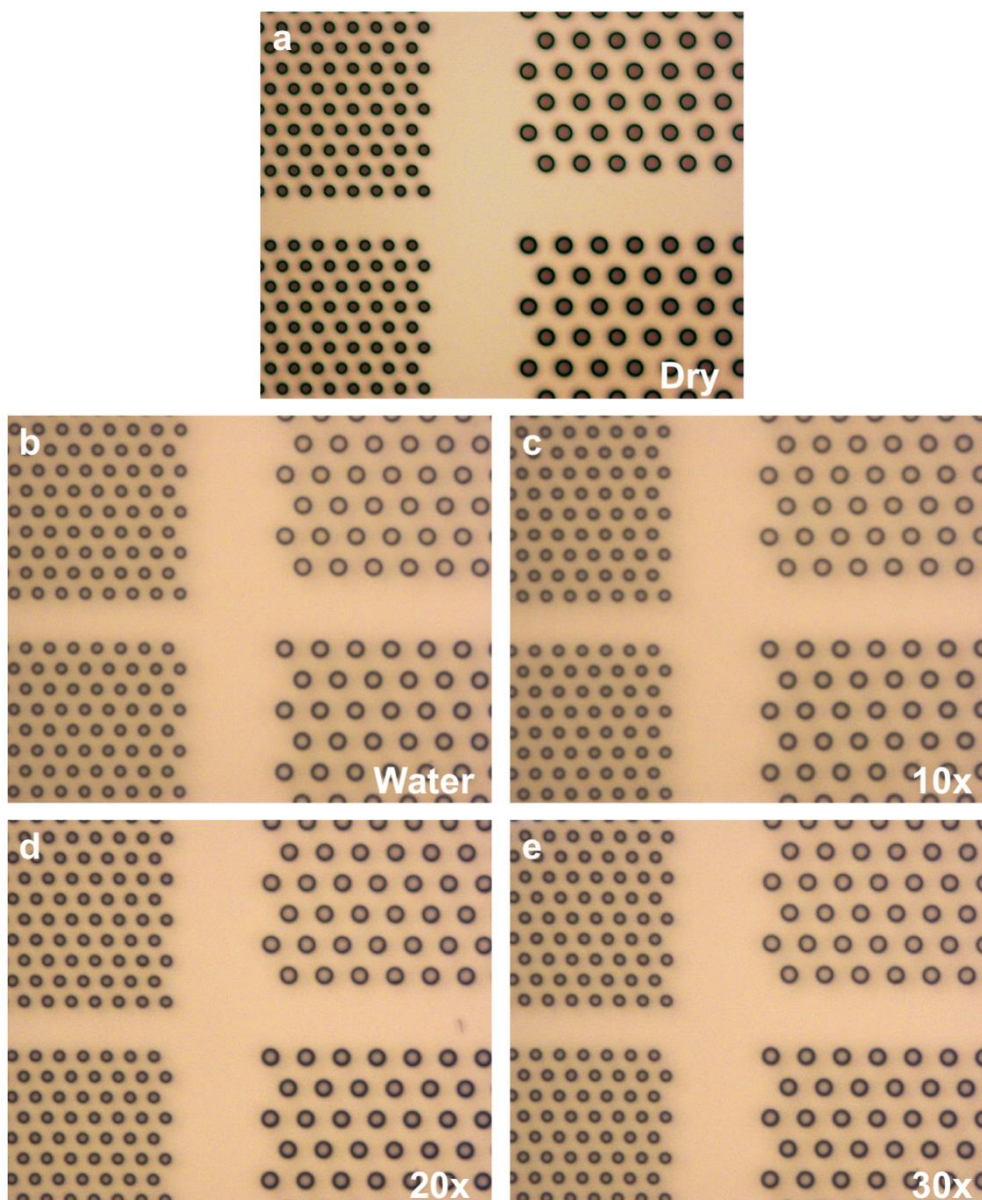
Supporting Figure S1. Additional experiment to address possible CNT detachment and/or destruction of the microstructures. a) A dry, undensified CNT sample. b) Water was added and the liquid was changed for 30 times while preventing the sample to dry out (c-e). This simulates considerably more turbulence than what would normally occur during a normal cell culture procedure. The results show that even undensified CNT forests remained firmly attached to the substrate.
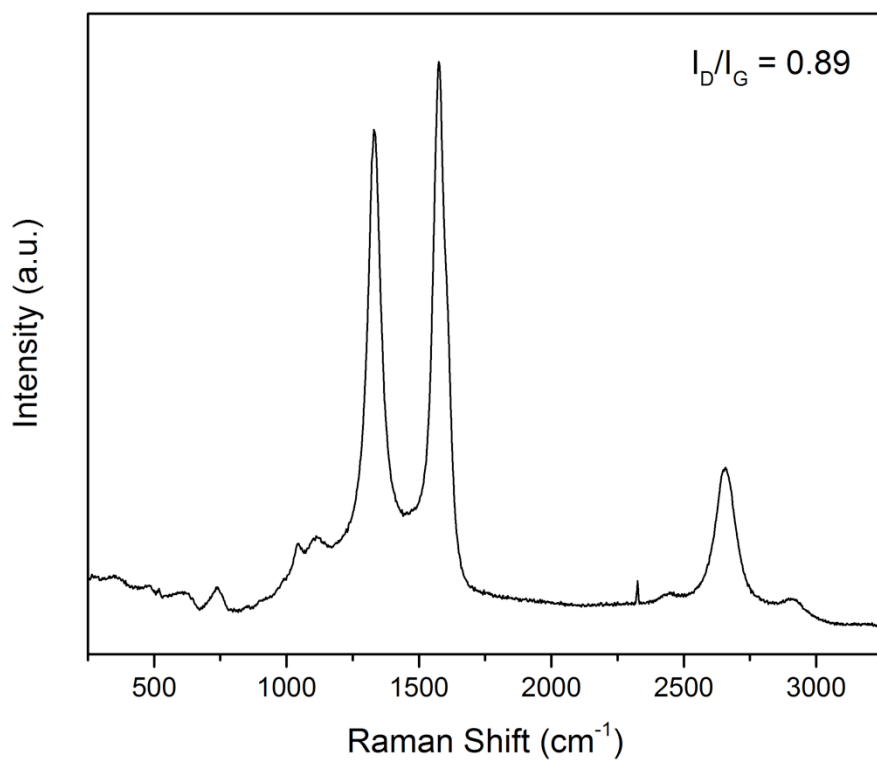
Supporting Figure S2. Raman spectrum of the as-grown multiwalled CNTs, with the three characteristic peaks at 1332 cm^{-1}, 1579 cm^{-1} and 2664 cm^{-1}.
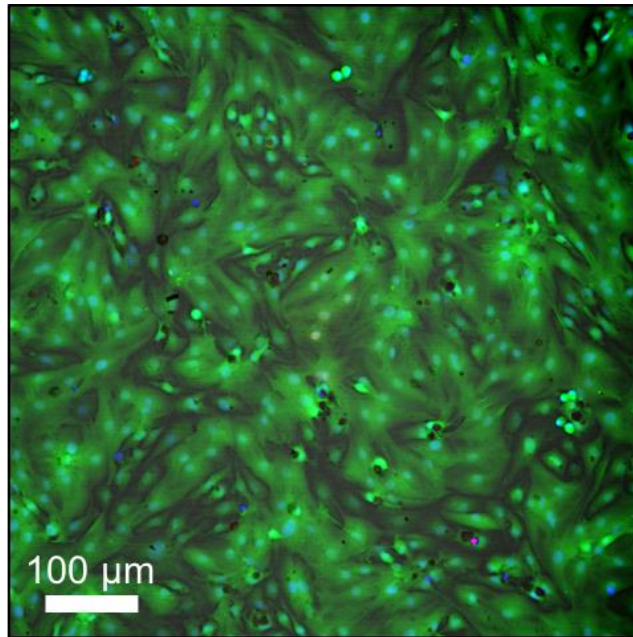
Supporting Figure S3. Fluorescence image of primary cardiomyocytes grown on top of flat Mo substrates at 3 DIV. Cell viability assay showing live cells stained with calcein (green) and dead cells with propidium iodide (red). Nuclei are stained with Hoechst (blue).
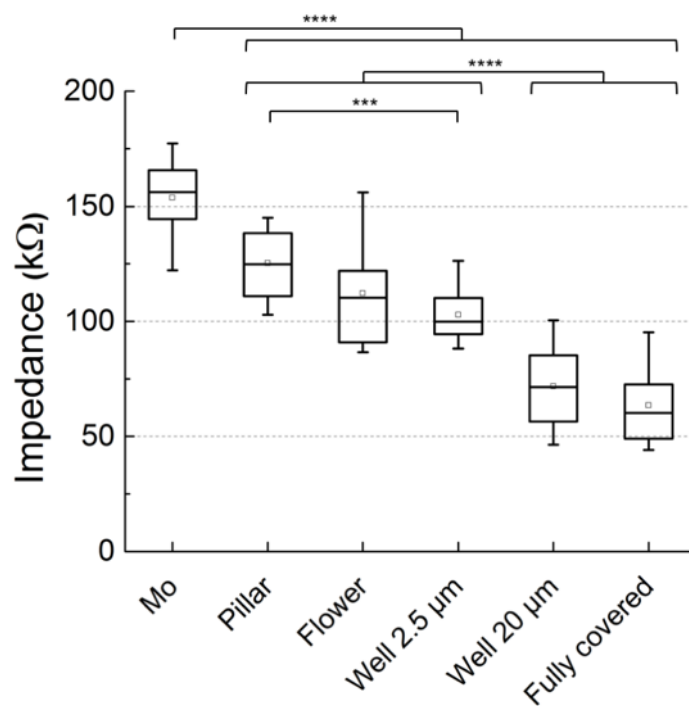
Supporting Figure S4. Electrochemical impedance spectroscopy data for bare, flat Mo and CNT structured electrodes. Box plots with median, 25th and 75th percentiles. Whiskers indicate 10th and 90th percentile. Asterisks indicate significant differences with $P<0.001$ (***) and $P<0.0001$ (****).
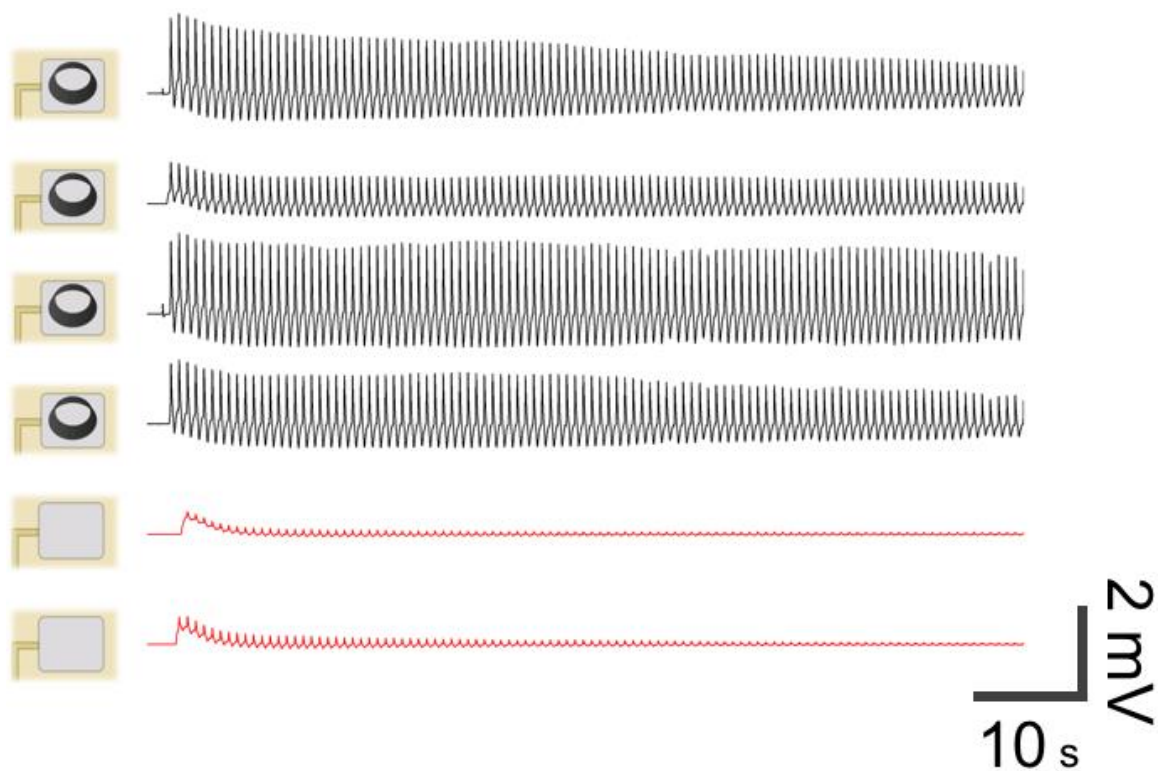
Supporting Figure S5. Example of a real-time recording after stimulation, with two Mo reference electrodes at the bottom and four electrodes with 20 μm CNT microwells on top.
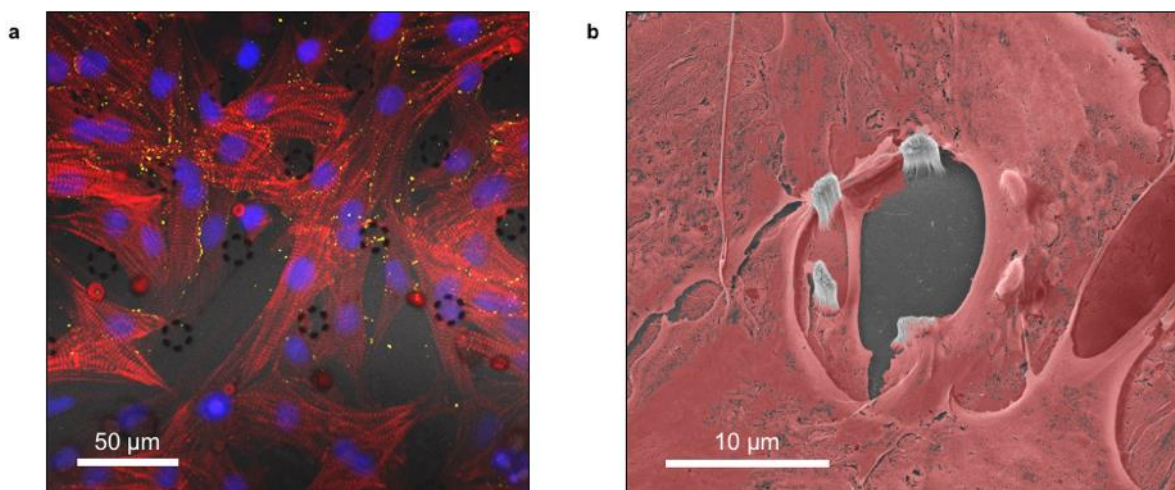
**Supporting Figure S6.** a) Confocal microscopy image of primary cardiomyocytes cultured on top of bent CNT pillars in a flower arrangement. α-actin filaments are stained in red, cell nuclei blue and the cardiac gap junction protein connexin-43 yellow. b) Colored SEM image of a primary cardiomyocyte in contact with a CNT 'flower'.
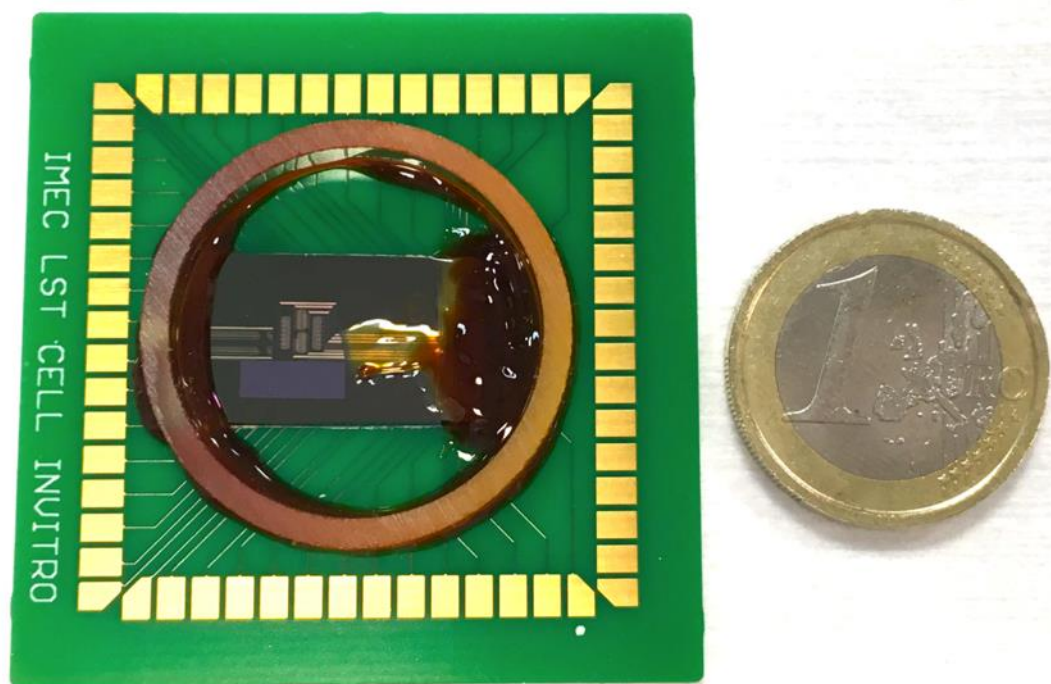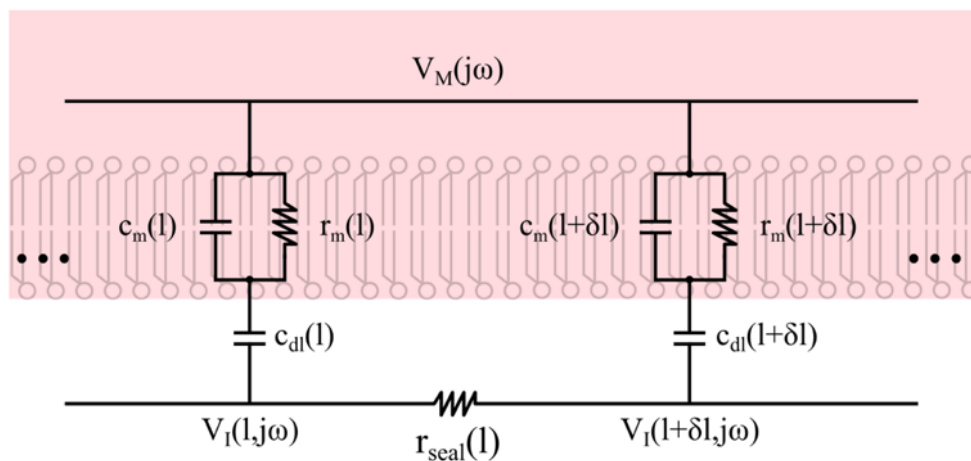
Supporting Figure S7. MEA chip wire-bonded to a PCB. Wires and part of the electrode lines are protected by a layer of biocompatible epoxy.
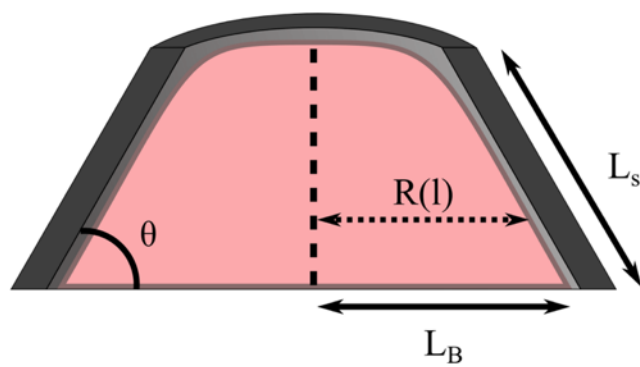
Supporting Figure S8. Cross-sectional schematic of a cell inside a microwell.

Supporting Figure S9. Area-contact model of the cell membrane. $V_M(j\omega)$ is the intracellular potential and $V_I(l,j\omega)$ the potential at the cell-electrode interface at a distance l from the center of the cell. c_m and r_m are the membrane capacitance and resistance, respectively. c_{dl} is the double-layer capacitance, r_{seal} the sealing resistance.
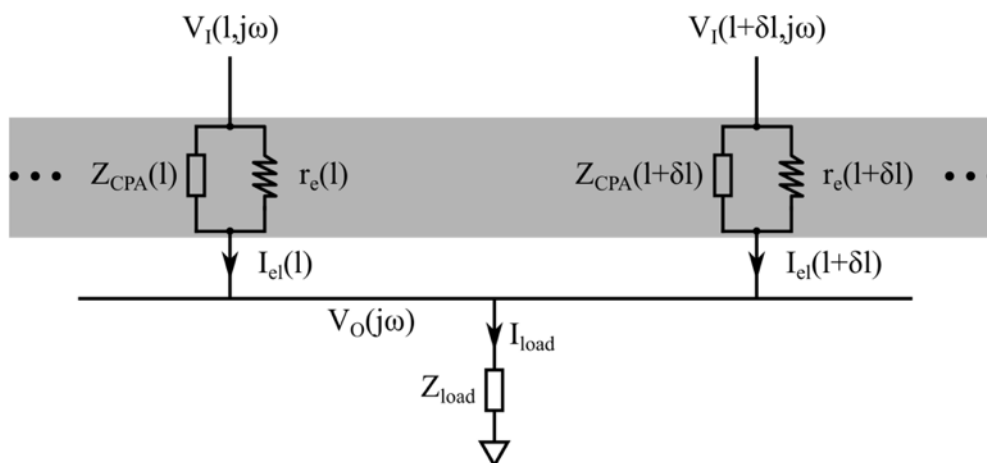
Supporting Figure S10. Area-contact model of the electrode. $V_I(l, j\omega)$ is the potential at the cell-electrode interface at a distance l from the center of the cell and $V_o(j\omega)$ the output potential of the electrode. Z_{CPA} is the constant phase angle element, r_e the electrode resistance, I_{el} the current flowing through the electrode, I_{load} the load current and Z_{load} the load impedance.

References

[1]   P. Fromherz, *Nanoelectron. Inf. Technol.* **2003**, *16*, 781.

[2]   N. Joye, A. Schmid, Y. Leblebici, *Neurocomputing* **2009**, *73*, 250.

[3]   A. Fendyur, N. Mazurski, J. Shappir, M. E. Spira, *Front. Neuroeng.* **2011**, *4*, 1.

[4]   P. Massobrio, G. Massobrio, S. Martinoia, *Neurocomputing* **2007**, *70*, 2467.

[5]   T. Kiss, *Acta Biochim Biophys Acad Sci Hung* **1977**, *12*, 291.

[6]   D. Braeken, D. Jans, R. Huys, A. Stassen, N. Collaert, L. Hoffman, W. Eberle, P. Peumans, G. Callewaert, *Lab Chip* **2012**, *12*, 4397.

[7]   W. Franks, I. Schenker, P. Schmutz, a Hierlemann, *IEEE T Bio-Med Eng* **2005**, *52*, 1295.

[8]   J. C. Padilha, E. M. A. Martini, C. Brum, M. O. de Souza, R. F. de Souza, *J. Power Sources* **2009**, *194*, 482.